Ore Geology Reviews 81 (2017) 256–269

Contents lists available at ScienceDirect

Ore Geology Reviews

journal homepage: www.elsevier.com/locate/oregeorev

Constraints of fluid inclusions and in-situ S-Pb isotopic compositions on the origin of the North Kostobe sediment-hosted gold deposit, eastern Kazakhstan

Kam-Hung Wong [a], Mei-Fu Zhou [a], Wei Terry Chen [b,*], Hugh O'Brien [c], Yann Lahaye [c], Sik-Lap Jacky Chan [a,d]

[a] Department of Earth Sciences, The University of Hong Kong, Hong Kong
[b] State Key Laboratory of Ore Deposit Geochemistry, Institute of Geochemistry, Chinese Academy of Sciences, Guiyang 550002, China
[c] Geological Survey of Finland, 02150 Espoo, Finland
[d] ProjecTerrae, Room 33, 23/F, On Hong Commercial Building, 145 Hennessy Rd, Wan Chai, Hong Kong

ARTICLE INFO

Article history:
Received 29 December 2015
Received in revised form 1 October 2016
Accepted 7 October 2016
Available online 15 October 2016

Keywords:
East Kazakhstan
Sediment-hosted gold
Orogenic gold
In-situ S and Pb isotopic analysis
LA-MC-ICP-MS

ABSTRACT

The North Kostobe gold deposit in the Kalba gold province, eastern Kazakhstan, is tectonically located in the Chara shear zone of the western Altaids. The Chara shear zone separates the Kazakhstan microcontinent and Siberia craton which collided in the late Carboniferous. In the North Kostobe deposit, Au mineralization is distributed along an E-W striking shear zone linked to the NW-SE trending regional faults, and is mainly concentrated in quartz-sulfide-carbonate veins or in disseminated sulfides hosted in carbonaceous metasedimentary rocks. Sulfide minerals are mainly pyrite and arsenopyrite, and were formed in three generations. The first generation is dominated by pyrite (py1) occurring as microcrystal aggregates, followed by the second generation including euhedral arsenopyrite and compact pyrite (py2) locally overgrowing early py1 grains as rims; third generation of pyrite (py3) is present in barren micro-fractures crosscutting early mineralized rocks. Native gold is present in cracks of brecciated arsenopyrite grains and as inclusions in py2. Investigations on fluid inclusions in auriferous quartz veins indicate that the ore-related fluids are CO_2-bearing, with homogenization temperatures of 288 °C and low salinity (1.42 to 8.03 wt% NaCl equiv). The fluids have calculated $\delta^{18}O$ and δD values ranging from 9.96 to 11.86‰ and from −75 to −97.1‰, respectively, suggesting that they were most likely metamorphic in origin.

The first and second generations of ore sulfides have similar $\delta^{34}S$ values (−6 to +2.6‰) which possibly indicating a common sulfur source as the hosting sedimentary rocks. In contrast, py3 grains have a huge range of $\delta^{34}S$ values (−40 to +54.5‰), indicating a biogenic source for the sulfur. On the other hand, in-situ Pb isotopic compositions of different generations of sulfides show a similarly mixed lead source, possibly involved orogen, mantle and lower crust Pb reservoirs. We propose that the gold-bearing fluids of the North Kostobe gold deposit were most likely derived from gold-rich, pyritic carbonaceous sedimentary rocks through dehydration during the metamorphism that was related to the collision between the Kazakhstan microcontinent and Siberia craton in the late Carboniferous. It is thus concluded that the North Kostobe gold deposit shares many characteristics with typical orogenic gold deposits in terms of tectonic settings, mineralization styles, fluid compositions and source of fluids and gold. Our new findings thus have important implications for regional exploration in the Kalba gold province.

1. Introduction

The Kalba gold province in eastern Kazakhstan is located in the western part of the Central Asian Orogenic Belt (CAOB), which is also known as the Altaids (Fig. 1a and b). The Kalba gold province hosts several large gold deposits, e.g. the Bakyrchik Au deposit (410 t Au; Goldfarb et al., 2014), the Sekisovskoye Au-Te deposit (160 t Au; resource statement of GoldBridges Global Resource Plc., 2014) and the Suzdal Au-As deposit (58 t Au; resource statement of Nord Gold, 2015). Exploration and mining activities in the province can be traced back to the 1950s by the Soviet geologists through systematic mapping, geophysical and soil geochemical surveys to target potential gold resources. Although the Kalba gold province hosts >450 gold deposits/occurrences, it only received little attention in the past owing to poor accessibility. Previous studies have mainly focused on mineralogy of gold and gold-bearing

* Corresponding author.
E-mail address: chenwei@mail.gyig.ac.cn (W.T. Chen).

http://dx.doi.org/10.1016/j.oregeorev.2016.10.004

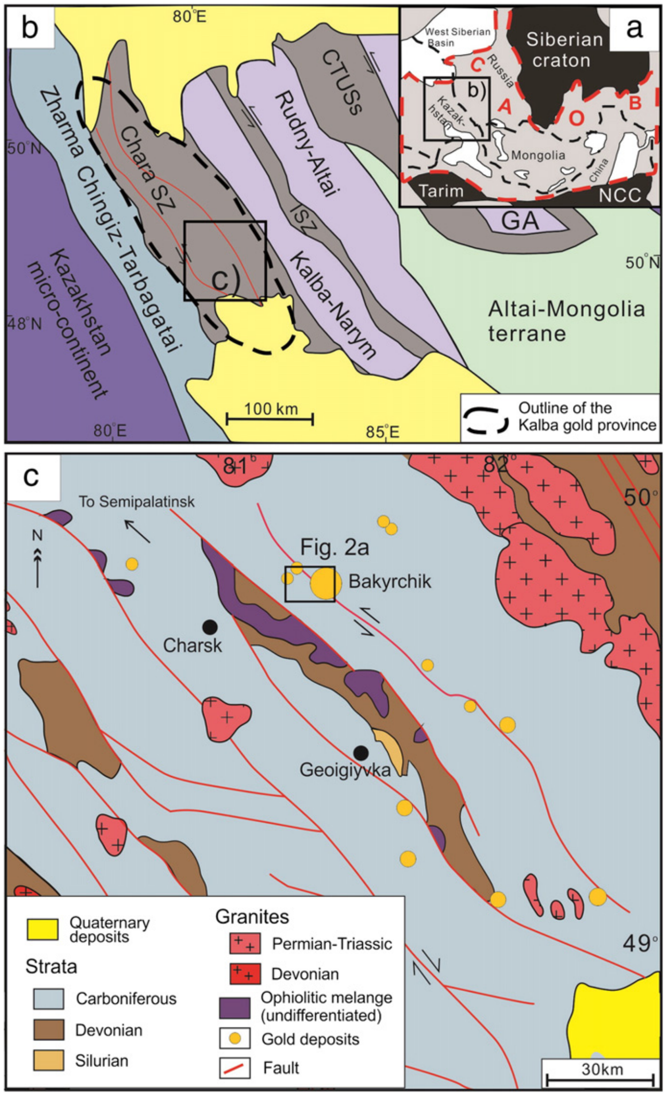

Fig. 1. a and b. Tectonic framework of the Central Asian Orogenic Belt and Kazakhstan microcontinent. ISZ = Irtysh shear zone, CTUSs = Charysh-Terekta-Ulagan-Sayan suture, GA = Gorny Altai, NCC = North China Craton. The outline of NW-SE trending Kalba gold province is also shown. Fig. 1a and b are modified after Glorie et al. (2012); c. Geological map of the Chara shear zone, simplified from Buslov et al. (2004), Daukeev et al. (2008).

sulfides (e.g., Kovalev et al., 2009, 2011, 2014; Kalinin et al., 2009; Kuz'mina et al., 2013), but the source of gold and the nature of the ore-forming fluids are currently poorly constrained.

This study provides a comprehensive description of the geology of the North Kostobe gold deposit, a medium tonnage gold deposit in the Kalba gold province, in order to constrain the origin of gold mineralization and in turn to provide a conceptual model for further exploration in the region. We obtained in-situ S and Pb isotopic compositions of sulfides by using the LA-MC-ICPMS technique that has high spatial resolutions, because the sulfides are fine-grained (<1 mm) and texturally complex, and may have formed in multiple stages (e.g. Large et al., 2007). Conventional fluid inclusions and H-O isotopic data of quartz are also incorporated in order to better constrain the origin of the deposit.

2. Regional geology

The Chara shear zone in CAOB was formed by the collision between the Siberia craton and the Kazakhstan microcontinent as a result of the closure of the Ob-Zaisan Ocean (part of the Paleo-Asian Ocean) in the late Carboniferous (e.g. Sengör et al., 1993; Buslov et al., 2001; Windley et al., 2007). It is several hundred kilometers long, NW-SE trending, and extends from eastern Kazakhstan to the Chinese Altai in Xinjiang, China (Li et al., 2015a). It is bounded by different terranes as a result of a series of accretionary events during the late Paleozoic (Buslov et al., 2001, 2004; Windley et al., 2007; Shen et al., 2016). The Chara shear zone separates the Siberia-derived Kalba-Narym (fore-arc accretionary complex), Rudny Altai and Gorny Altai terranes (island arc systems) and the Kazakhstan-derived active margin of the Zharma-Chingiz-Tarbagatai terrane (Berzin et al., 1994; Buslov et al., 2001) (Fig. 1b).

The Chara shear zone (Fig. 1c) is marked by three types of ophiolitic mélange of different origins (Buslov et al., 2004): 1) the Cambrian to early Ordovician mélange composed of high-pressure metamorphic rocks and gabbro (Buslov et al., 2003; Volkova et al., 2008), 2) the Ordovician mélange containing blocks of serpentinized peridotite, gabbro, and amphibolite (Iwata et al., 1997; Safonova et al., 2012), and 3) the Carboniferous to early Permian NW-SE oriented ophiolitic mélange representing the lithospheric fragments of the Ob-Zaisan Ocean closed in the late Carboniferous (Iwata et al., 1997; Buslov et al., 2001, 2004). These ophiolite mélanges are associated with 5000-m-thick Silurian to Carboniferous sedimentary successions (Safonova et al., 2012). These successions are fore-arc materials derived from both the Kazakhstan microcontinent and Siberia craton during the evolution of the Ob-Zaisan Ocean (Buslov et al., 2004). The Silurian strata are mainly composed of alternating limestone, siltstone and chert, whereas the Upper Devonian strata are mainly dominated by chert and siltstone with minor amounts of pillow basalts (Iwata et al., 1997). These sequences are overlain by Carboniferous fore-arc turbidite and intermediate to felsic volcanic rocks that define an active continental margin in the Carboniferous. Intrusions in the Chara shear zone are rarely exposed, and those that do occur are present as small plutons and dyke complexes. They have mostly formed between the late Carboniferous and Triassic (Lyons et al., 2002; Vladimirov et al., 2008).

The Chara shear zone is characterized by complex regional scale folding, shearing and faulting with a NW-SE trend. The deformation has created foliations in the rocks and juxtaposed, different geological units. Large-scale strike-slip faults were activated during the Permian. The timing of sinistral deformation of the Irtysh shear zone in the Kazakhstan segment, which is situated ~80 km northeast to the study area, is constrained to be ~290 to 265 Ma (Travin et al., 2001; Buslov et al., 2004, and references therein; Vladimirov et al., 2008) although the Irtysh shear zone was reactivated in the Mesozoic (Yuan et al., 2006; Glorie et al., 2012). Sinistral strike-slip deformation of the Chara shear zone was most likely coeval with the Irtysh shear zone (Li et al., 2015b). Some workers have suggested that such events are likely related to the collision between the Siberia craton and the Kazakhstan microcontinent and their differential rotations with respect to the major continental blocks (Didenko et al., 1994; Buslov et al., 2001, 2003).

Numerous gold deposits are distributed along the Chara shear zone, defining the Kalba gold province. Naumov et al. (2012) and Kovalev et al. (2009) reported $^{40}Ar/^{39}Ar$ and SHRIMP U-Pb ages of some selected gold deposits in the Kalba province, ranging from 306.6 ± 3.8 Ma to 248.3 ± 3.4 Ma. These ages suggest that the mineralization was synchronous with the deformation in the Irtysh shear zone as well as the major episode of emplacement of post-collisional granitoids in the Kalba-Narym terrane (295 to 274 Ma) (Vladimirov et al., 2008). However, it is not clear whether the gold mineralization was genetically related to igneous activity in the Kalba gold province (Kovalev et al., 2014).

3. Deposit geology

The North Kostobe gold deposit is located in the Bakyrchik ore district of the Kalba gold province (Fig. 2). In the district, NW-trending

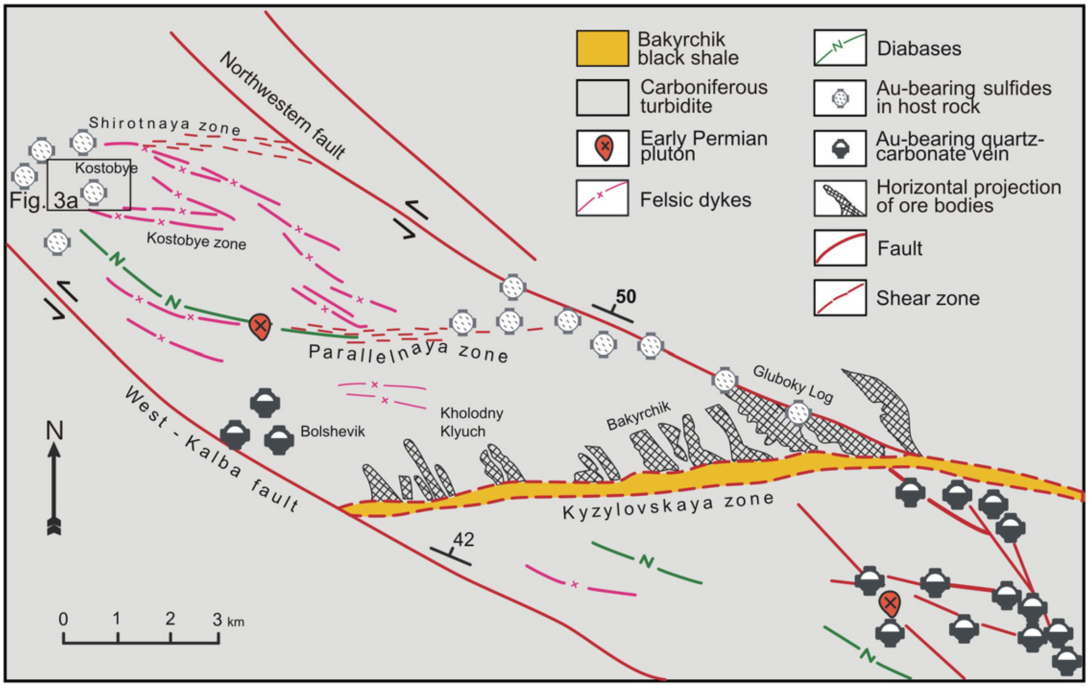

Fig. 2. Geological map of the Bakyrchik ore field. Simplified from Daukeev et al. (2004).

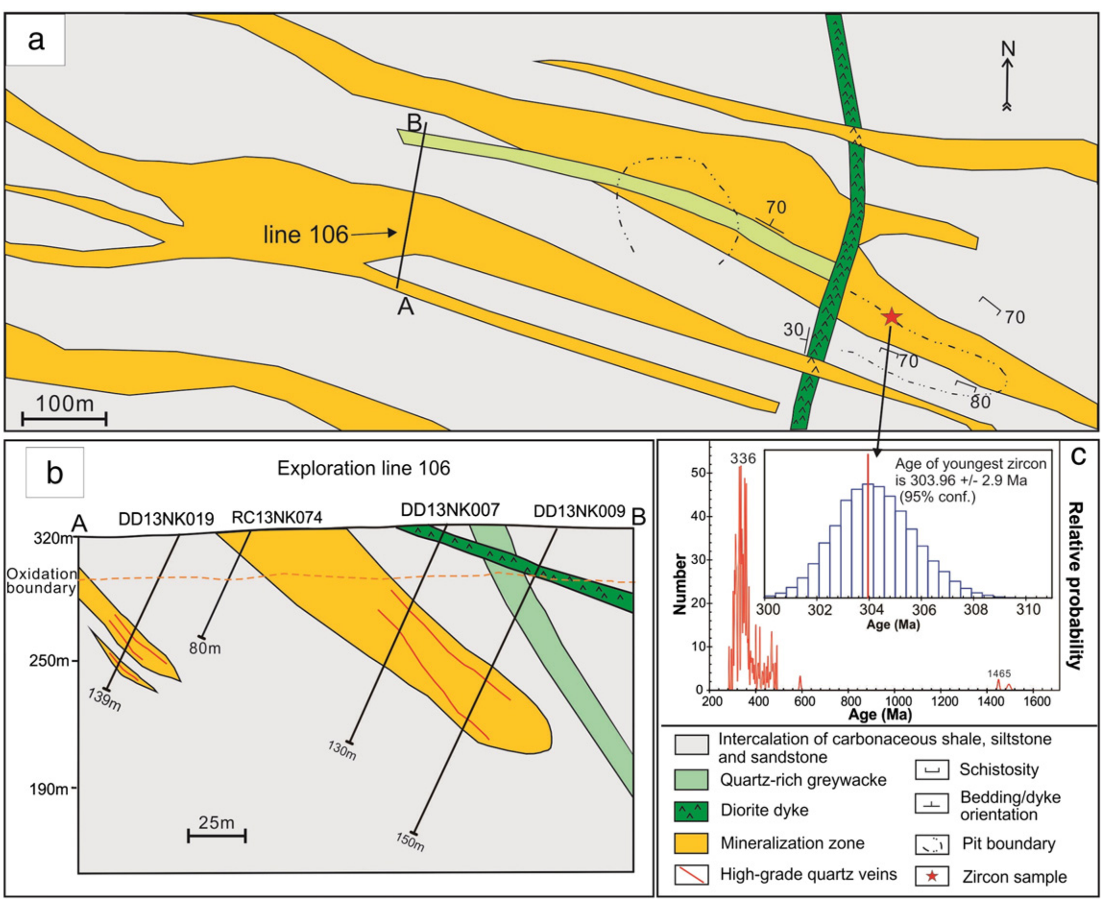

Fig. 3. a. Geological map of the North Kostobe gold deposit; b. Cross section of exploration line 106, showing major drill holes intersection (Modified from IRG maps); c. relative probability plot of detrital zircon age of the greywacke host rocks. Calculation of the youngest zircon by isoplot v.4.15 (Ludwig, 2008).

regional thrust faults, the West Kalba fault and Northwestern fault, gently dip towards NE. Mineralization is structurally controlled by a series of E-W oriented, moderately dipping shear zones conjugate to these thrust faults (Gosselin and Dubé, 2005). The age of the North Kostobe deposit is not available currently, but the Bolshevik gold deposit in the same ore district has an ^{40}Ar-^{39}Ar age of 285.6 ± 3.3 Ma (Naumov et al., 2012) which provides an estimate for the timing of the gold mineralization for the North Kostobe gold deposit.

3.1. Host rocks

Mineralization zones of the North Kostobe deposit are mostly covered by Quaternary sediments, with limited exposures in the historical mine pit and trenches (Fig. 3a). The mineralization zones are NWW-SEE trending, lenticular in shape and dipping north (Fig. 3b). Mineralization is hosted in Carboniferous sandstone, siltstone and carbonaceous shale, which have undergone low-grade metamorphism. The host rocks, locally containing disseminated pyrite grains (Fig. 4b), are commonly foliated, but steep bedding of these rocks is revealed by a white, quartz-rich greywacke layer which is NW-trending and dips NE (Fig. 4c). Our U-Pb ages of detrital zircon from the host rocks indicate that the maximum depositional age is ~304 Ma (Fig. 3c) (analytical method of zircon U-Pb ages is presented in Appendix A. S1). The metasedimentary host rocks are crosscut by a diorite dyke which dips gently to the west (Fig. 4d). The exact age of the dyke is unknown but it pre-dates the gold mineralization as it is mineralized.

3.2. Alteration and mineralization

Hydrothermal alteration of the black shales is usually weak and occurs as halos around veins. Widths of alteration halos vary from millimeters to meters (Fig. 4e and f). On the other hand, the alteration on the sandstone and siltstone is marked by bleaching/discoloration of wall rocks to pale grey or pale-greenish grey due to the formation of sericite ± carbonate ± quartz.

Gold mineralization is closely associated with sulfide minerals occurring in fault-related quartz-carbonate veins or as disseminations in wall rocks (Fig. 4g and h). The auriferous quartz-carbonate veins are monomictic and meters thick, and contain host rock fragments and fine-grained sulfide minerals. High-grade Au mineralization (generally >10 g/t) is present in the quartz-carbonate veins, whereas lower-grade mineralization (<1 to 10 g/t) is present in sulfide disseminations distributed in the halo surrounding the veins (Fig. 5).

Based on field and drill core observations, it is indicated that oxidized zones typically extend from the surface to <30 m depth. Fe-oxides and remnants of pyrite and arsenopyrite are commonly found in these oxidized ores. Finely dispersed native copper and gold grains can also be found in the matrix.

Fig. 4. a. high angle schistosity in metasedimentary host rocks in the mine pit. The orange and brown colors are due to oxidation; b. trace of fine-grained pyrite in the metasedimentary host rocks; c. quartz-rich greywacke layer in a metasedimentary unit. NWW-SEE strike with steep bedding; d. N-S oriented diorite dyke within a metasedimentary unit; e. restricted alteration envelops surrounding veins in carbonaceous wall rock. Alteration is characterized by bleaching to pale greenish/ grey colour; f. pervasive alteration in greywacke surrounding auriferous vein, including predominantly silicification, sericite, carbonate alteration; g. quartz-carbonate breccia vein with high gold grade, composed of wall rocks fragments cemented by quartz; h. disseminated sulfides in host black shale.

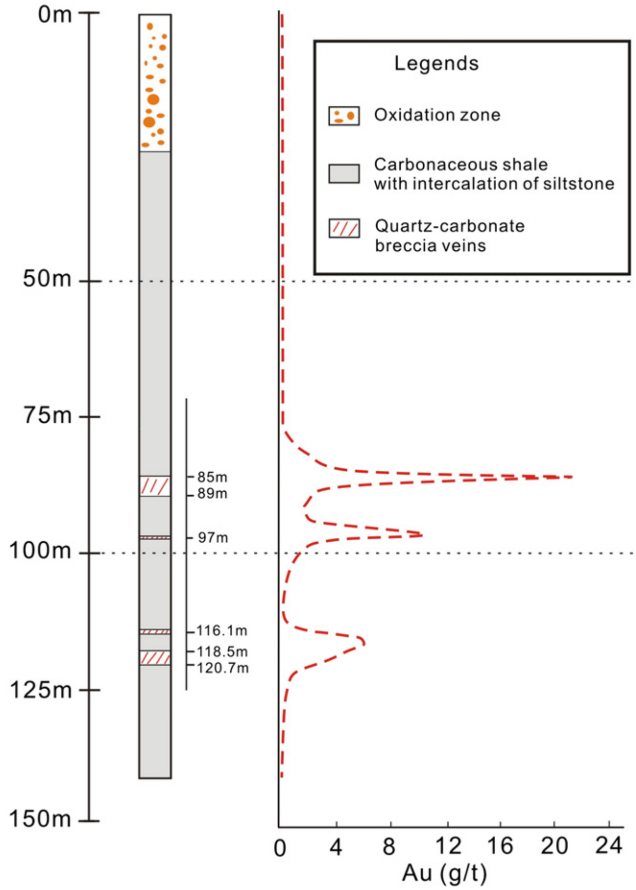

Fig. 5. Schematic diagram of drillhole DD13NK019, showing variation of gold grade with depth and positions of quart-carbonate breccia veins. Au grade reaches the highest at the quartz-carbonate breccia veins and decreases away from the vein center. Source of data is from IRG.

4. Mineralogy of sulfides

Sulfides related to the Au mineralization are dominantly pyrite and arsenopyrite with minor chalcopyrite, galena and sphalerite. There are three generations of sulfides. The first generation includes pyrite (py1) grains occurring as microcrystal aggregates (Fig. 6a) disseminated in carbonaceous host rocks. They are irregular in shape, varying from 100 to 500 μm in diameter. Py1 contains variable amounts of Au (up to 0.08 wt%) and As (up to 2.88 wt%) (Appendix A. S2 and S3). The texture of the py1 is similar to that of diagenetic pyrite in (Thomas et al., 2011).

The second sulfide generation is volumetrically dominant and composed of pyrite (py2) and arsenopyrite. The py2 grains are generally compact without pores. They occur as euhedral to sub-euhedral grains (<1 mm) disseminated in host rocks or as rims overgrowing py1 microcrystal aggregates (Fig. 6b). The py2 grains contain up to 0.04 wt% Au and 5.25 wt% As (Appendix A. S2 and S3). Au in py2 mostly occurs as lattice bound Au although native gold inclusions are also present (Fig. 6c). Arsenopyrite co-existing with py2 (Fig. 6g) is fine-grained (usually hundreds of μm in size), and has generally shapes of lozenges, long prisms or acicular forms (Fig. 6d). Arsenopyrite contains variable amounts of Au up to 0.44 wt%. In some samples, native gold occurs as irregular grains (1 to 10 μm in width) along cracks and as inclusions within brecciated arsenopyrite (Fig. 6e and f). The third generation of sulfides are dominated by euhedral to sub-euhedral pyrite (py3) occurring in micro-fractures (<1 mm) that crosscut the mineralized rocks (Fig. 6h).

5. Analytical methods

5.1. In-situ sulfur isotope analysis

Sulfur isotope analyses of pyrite were performed using a Nu-Plasma HR multicollector ICP-MS together with a Photon Machine Analyte G2 laser ablation system at the Geological Survey of Finland, Espoo, Finland. Samples were ablated in He gas (gas flows = 0.4 and 0.1 min^{-1}) within a HelEx ablation cell (Müller et al., 2009). Sulfur isotopes were analyzed at medium resolution. During the ablation, the data were collected in static mode (^{32}S, ^{34}S).

Pyrites were ablated by laser with spot size diameter of 50 μm using a fluence of 0.83 J/cm^2 and at 5 Hz. The total S signal obtained for pyrite was typically 1.9–2.3 V. Under these conditions, after a 20 s baseline, 50–60 s of ablation was needed to obtain an internal precision of ^{34}S/^{32}S ≤ ± 0.000005 (1SE). Two pyrite standards were used for external standard bracketing PPP-1 (Gilbert et al., 2014) and in-house Py2 for quality control of analysis. We have measured an average $\delta^{34}S_{CDT}$ (‰) value of −0.22 ± 0.35 (1σ, n = 35) for the in-house Py2 standard using the LA-MC-ICPMS method. This value is within uncertainty of the $\delta^{34}S_{CDT}$ (‰) value of −0.4 ± 0.5‰ (1σ) of the in-house Py2 measured by gas mass spectrometry.

5.2. In-situ lead isotope analysis

In-situ lead isotopic analyses of pyrite and chalcopyrite were conducted on 50–100-μm-thick polished sections, using a Nu Plasma™ multi-collector ICPMS with a femtosecond laser ablation system (NWR UPFemto, ESI, USA) (fLA-MC-ICPMS) at the State Key Laboratory of Continental Dynamics, Northwest University, Xian, China. Detailed description of the measuring procedures is available in Chen et al. (2013) and Yuan et al. (2015). Argon and helium were used as the carrier gases for laser ablation. The aerosol from the ablation cell was mixed with Tl (argon with Tl) in a glass aerosol homogenizer and then introduced into the ICP for atomization and ionization. During the instrumental analysis, the intensities of the ion beams of ^{202}Hg, ^{203}Tl, ^{204}Pb + Hg, ^{205}Tl, ^{206}Pb, ^{207}Pb and ^{208}Pb were simultaneously monitored with the Faraday collectors L4, L3, L2, L1, Ax, H1 and H2, respectively. The concentrations of lead and mercury in the gas blank were lower than 10 and 20 pg/l, respectively, and thus their contributions for the analyses were negligible. Thallium was used to monitor and correct for instrumental mass discrimination, and ^{202}Hg was used to correct for the isobaric overlap of ^{204}Hg on ^{204}Pb. The calculated and determined interference of ^{204}Hg on ^{204}Pb was achieved using the natural abundance ratio ^{204}Hg/^{202}Hg = 0.229883 (^{202}Hg = 0.29863 and ^{204}Hg = 0.06865) adjusted for instrumental mass fractionation as monitored by the ^{205}Tl/^{203}Tl ratio. The ^{204}Hg/^{204}Pb ratios varied from day to day, but they were <20 ppm in the experimental system when the ion beam of ^{204}Pb had intensity >0.25 V.

The acquisition of the MC-ICP-MS data employed the time-resolved analysis (TRA) mode with an integration time of 0.2 s, and laser ablation was performed in the line scan ablation mode at a speed of 5 μm/s with the laser beam focused on the sample surface. Each line scan analysis consisted of background collection for 40 s followed by an additional 50 s of ablation for signal collection and 40 s of wash time to reduce memory effects and to allow the instrument to stabilize after each analysis. All of the recorded Pb and Hg signals were corrected for background by subtracting the background signals (gas blank and dark noise signals) from the corresponding gross signals (signals obtained after firing the laser), whereas the Tl signals were corrected for background by subtracting the average dark noise signals (stability <25 ppm at 10 min). To ensure the stability of ^{208}Pb signal obtained from different samples with disparate Pb concentrations, samples were ablated with laser line scans approximately 120 μm in length and 30–65 μm in width with adjustable laser frequency. NIST SRM 610 was used as a quality control sample (Yuan et al., 2013), and was analyzed once for every five sample points (Appendix A. S4). The obtained average values

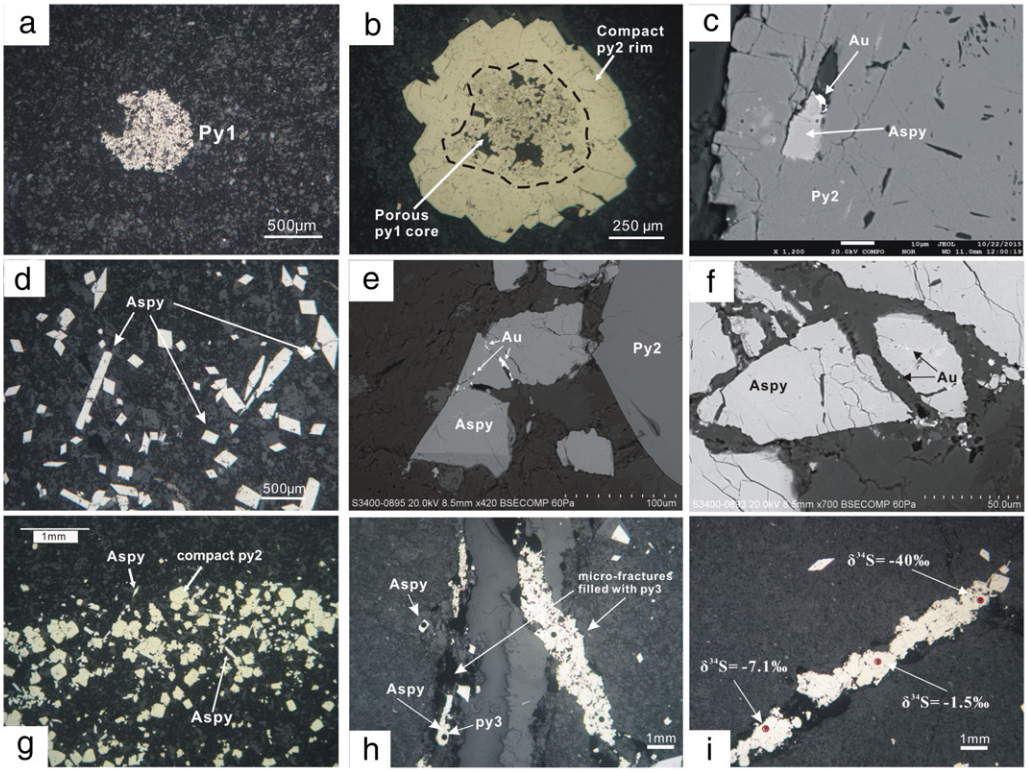

Fig. 6. Three generations of sulfides were identified in this study: a. py1 microcrystals aggregates; b. porous py1 core overgrown by later compact py2; c. BSE image showing native gold associated with arsenopyrite and compact py2; d. examples of different shapes of arsenopyrite grains; e and f. BSE images of brecciated arsenopyrite where native gold deposited along the cracks of fractured grain or as inclusion in the arsenopyrite; g. coexisting compact py2 grains and arsenopyrite; h. py3 in micro-fractures crosscutting mineralized rocks. py3 is also rimming the arsenopyrite; i. extreme $\delta^{34}S$ variation in py3 (see Section 7.1.2).

of Pb isotopic compositions of NIST SRM 610 in this study are: $^{208}Pb/^{204}Pb = 36.981 \pm 0.004$; $^{207}Pb/^{204}Pb = 15.515 \pm 0.001$; $^{206}Pb/^{204}Pb = 17.052 \pm 0.001$ (1σ), similar to the reference values of NIST SRM 610: $^{208}Pb/^{204}Pb = 36.964 \pm 0.022$; $^{207}Pb/^{204}Pb = 15.504 \pm 0.001$; $^{206}Pb/^{204}Pb = 17.045 \pm 0.008$ (2σ) (Jochum and Stall, 2008).

5.3. Fluid inclusion microthermometry

Microthermometric measurements were carried out on fluid inclusions in auriferous quartz veins at the Guangzhou Institute of Geochemistry, Chinese Academy of Sciences, using a Linkam TH600 heating–freezing stage which is attached to a Leitz Ortholux transmitted light microscope connected to a television camera and screen. The stage was calibrated using synthetic fluid inclusions. The estimated accuracy was ±0.1 °C at temperatures below 30 °C and ±1 °C at temperatures above 30 °C. The warming rate was maintained from 0.2 °C to 5 °C min^{-1}, and the heating rate was reduced to 0.2 °C min^{-1} when approaching phase-change conditions. Direct freezing to −90 °C was performed first on all sections to avoid decrepitation of inclusions at high temperature.

5.4. Oxygen and hydrogen isotope analyses

Oxygen isotope analyses were carried out on 10 to 20 mg of quartz using the BrF_5 method (Clayton and Mayeda, 1963). The precision for $\delta^{18}O$ is 0.2‰. Hydrogen isotope compositions of fluid inclusions were analyzed using the Zn reduction method (Colemen et al., 1982). The precision is 0.2‰ for natural water and 0.3‰ for fluid inclusions. A MAT253-EM mass spectrometer was used for oxygen and hydrogen isotope analysis at the Analytical Laboratory in Beijing Research Institute of Uranium Geology, China National Nuclear Corporation (CNNC). Isotopic fractionation between quartz and water was calculated using the equation, $1000\ln\alpha = 3.38 \times 106 / T^2–3.4$ (Clayton et al., 1972), at the minimum trapping temperature, which was defined by the average homogenization temperatures of fluid inclusions for quartz samples.

6. Results

6.1. In-situ sulfur isotopic compositions

In-situ S isotopic compositions of sulfides are listed in Table 1. The py1 grains have $\delta^{34}S$ values of −4.5 to +2.6‰ (30 analyses), comparable to the py2 grains (−6.0 to +0.2‰; 45 analyses) and arsenopyrite grains (−3.6 to +1.9‰; 24 analyses) of the second generation. In contrast, py3 grains in the micro-fractures have an extremely large range of $\delta^{34}S$ values from −40 to +54.5‰ (15 analyses).

6.2. In-situ lead isotopes

Lead isotopic compositions of sulfides are listed in Table 2. The py1 grains have $^{206}Pb/^{204}Pb$, $^{208}Pb/^{204}Pb$ and $^{207}Pb/^{204}Pb$ ratios ranging from 17.944 to 18.118 (average of 17.99), 37.600 to 37.715 (average of 37.673) and 15.433 to 15.485 (average of 15.472), respectively. The py2 grains have $^{206}Pb/^{204}Pb$ values from 17.976 to 19.249 (average of 18.106), $^{208}Pb/^{204}Pb$ values from 37.556 to 38.243 (average of 37.735) and $^{207}Pb/^{204}Pb$ values from 15.419 to 15.554 (average of 15.476), similar to arsenopyrite with $^{206}Pb/^{204}Pb$, $^{208}Pb/^{204}Pb$ and $^{207}Pb/^{204}Pb$

Table 1
In-situ sulfur isotopic composition of sulfides from the North Kostobe gold deposit.

Analysis_ID	Minerals	δ^{34}S‰ CDT	2σ
09-87.7-py1	Py2	−4.7	0.17
09-87.7-py2	Py2	−2.42	0.2
09-87.7-py3	Py2	−1.59	0.21
09-87.7-py4	Py2	−1.33	0.46
09-87.7-py5	Py2	−2.47	0.2
09-87.7-py6	Aspy	−2.02	0.62
09-87.7-py7	Aspy	−0.58	0.49
09-87.7-py8	Py2	−1.92	0.32
09-98.4-py1	Py2	−0.21	0.17
09-98.4-py10	Py2	0.16	0.21
09-98.4-py2	Py2	−0.11	0.15
09-98.4-py3	Py2	−3.48	0.16
09-98.4-py4	Py2	−2.29	0.16
09-98.4-py5	Py2	−3	0.16
09-98.4-py6	Py2	−2.57	0.16
09-98.4-py7	Py2	−0.29	0.16
09-98.4-py8	Aspy	−1.73	0.41
09-98.4-py9	Py2	0.12	0.16
11-111.3-py1	Aspy	−0.29	0.45
11-111.3-py2	Aspy	1.41	0.52
11-111.3-py3	Aspy	−0.28	0.55
11-111.3-py4	Aspy	−0.98	0.52
11-111.3-py5	Py3	−2.76	0.52
11-111.3-py6	Py3	−21.87	0.35
11-111.3-py7	Aspy	−0.02	0.58
11-111.3-py8	Py3	33.16	0.52
11-111.3-py9	Py3	44.66	0.74
11-111.3-py10	Py3	42.37	0.58
19-86.2-py1	Aspy	−0.44	0.55
19-86.2-py2	Py2	−0.67	0.34
19-86.2-py3	Aspy	−1.35	0.18
19-86.2-py4	Py2	−0.89	0.18
19-86.2-py5	Py2	−1.16	0.18
19-86.2-py6	Py2	−1.17	0.14
19-86.2-py7	Py2	−1.19	0.16
19-86.2-py8	Py2	−1.37	0.15
09-82.6-py1	Py2	−4.33	0.17
05-90.2-aspy1	Aspy	1.08	0.22
05-90.2-aspy2	Aspy	0.05	0.21
05-90.2-aspy3	Aspy	1.20	0.17
05-90.2-aspy4	Aspy	1.89	0.23
07-61.5-py1	Py2	−0.61	0.14
07-61.5-py2	Py2	−3.07	0.15
07-61.5-py3	Py2	−3.07	0.14
07-61.5-py4	Py2	−2.74	0.14
07-61.5-py5	Py1 (core)	2.57	0.14
07-61.5-py6	Py2 (rim)	−2.73	0.19
07-61.5-py7	Py2	−1.58	0.15
07-61.5-aspy1	Aspy	−3.64	0.25
07-61.5-aspy2	Aspy	−1.20	0.24
07-61.5-aspy3	Aspy	−1.24	0.34
07-61.5-aspy4	Aspy	−2.91	0.19
07-61.5-aspy5	Aspy	−2.38	0.21
05-88.6-py1	Py1 (core)	−0.20	0.16
05-88.6-py2	Py1 (core)	0.27	0.14
05-88.6-py3	Py2 (rim)	−2.39	0.14
05-88.6-py4	Py1 (core)	0.05	0.15
05-88.6-py5	Py2 (rim)	−2.00	0.17
05-88.6-py6	Py1 (core)	0.99	0.15
05-88.6-py7	Py2 (rim)	−0.36	0.17
05-88.6-aspy1	Aspy	−0.44	0.26
05-88.6-aspy2	Aspy	−1.22	0.30
05-88.6-aspy3	Aspy	−1.55	0.21
05-88.6-aspy4	Aspy	−0.99	0.25
05-88.6-aspy5	Aspy	−0.89	0.23
19-96.9-py1	Py2 (rim)	−2.85	0.14
19-96.9-py2	Py1 (core)	−1.79	0.15
19-96.9-py3	Py1 (core)	−1.93	0.14
19-96.9-py4	Py1 (core)	−1.90	0.13
19-96.9-py5	Py2 (rim)	−2.43	0.13
06-60.6-py1	Py1 (core)	−1.32	0.15
06-60.6-py2	Py1 (core)	−4.46	0.15
06-60.6-py3	Py1 (core)	−2.03	0.17
06-60.6-py4	Py1 (core)	−0.53	0.14
06-60.6-py5	Py2	−6.02	0.15
06-60.6-py6	Py2	−3.80	0.27
07-55.5-(2)-py1	Py1 (microcrystals aggregate)	−2.56	0.15
07-55.5-(2)-py2	Py1 (microcrystals aggregate)	−1.39	0.16
07-55.5-(2)-py3	Py1 (microcrystals aggregate)	−2.28	0.14
07-55.5-(2)-py4	Py1 (microcrystals aggregate)	−1.26	0.18
07-55.5-(2)-py5	Py1 (microcrystals aggregate)	−1.73	0.19
07-55.5-(2)-py6	Py1 (microcrystals aggregate)	−0.66	0.66
07-55.5-(2)-py7	Py1 (microcrystals aggregate)	−1.76	0.15
07-55.5-(2)-py8	Py1 (core)	−2.55	0.15
07-55.5-(2)-py9	Py2	−3.42	0.15
07-55.5-(2)-py10	Py2	−2.91	0.14
07-55.5-(2)-py11	Py1 (core)	−3.08	0.15
07-55.5-(2)-py12	Py1 (microcrystals aggregate)	−0.60	0.15
07-55.5-(2)-py13	Py1 (core)	−2.58	0.15
07-55.5-(2)-py14	Py1 (core)	−2.69	0.14
07-55.5-(1)-py1	Py1 (core)	−2.40	0.15
07-55.5-(1)-py2	Py1 (microcrystals aggregate)	−1.45	0.24
07-55.5-(1)-py3	Py1 (core)	−2.57	0.16
07-55.5-(1)-py4	Py1 (core)	−1.70	0.17
07-55.5-(1)-py5	Py2 (rim)	−3.16	0.15
07-55.5-(1)-py6	Py2 (rim)	−3.03	0.13
07-55.5-(1)-py7	Py1 (core)	−1.95	0.14
07-55.5-(1)-py8	Py2 (rim)	−3.29	0.14
07-55.5-(1)-py9	Py2	−3.20	0.16
07-55.5-(1)-py10	Py2 (rim)	−3.39	0.17
07-55.5-(1)-py11	Py1 (core)	−1.83	0.17
07-55.5-(1)-py12	Py2 (rim)	−2.67	0.13
11-111.3 Aug-py1	Py3	−4.70	1.76
11-111.3 Aug-py2	Py3	−4.11	2.20
11-111.3 Aug-py3	Py3	−1.37	0.16
11-111.3 Aug-py4	Py3	54.46	0.79
11-111.3 Aug-py5	Py3	7.97	3.54
11-111.3 Aug-py6	Py3	−19.11	1.93
11-111.3 Aug-py7	Py3	37.78	1.12
11-111.3 Aug-py8	Py3	−39.99	0.80
11-111.3 Aug-py9	Py3	−1.52	0.17
11-111.3 Aug-py10	Py3	−7.11	0.66
11-111.3 Aug-py11	Py2	−1.61	0.17
11-111.3 Aug-py12	Py2	−0.39	0.17

Aspy: arsenopyrite; Py: pyrite.

ratios ranging from 17.8 to 19.346 (average of 18.225), 37.268 to 38.13 (average of 37.722) and 15.321 to 15.589 (average of 15.459), respectively.

6.3. Fluid inclusions

Fluid inclusions in quartz from auriferous veins are small in size (<10 μm). They occur generally as clusters and trails within the growth zone of the quartz grains (Fig. 7a), and thus are mostly considered to be pseudo-secondary in origin. There are CO_2-H_2O inclusions (Fig. 7b and b′) with CO_2 phases mostly accounting for 15% to 35% of the volume but ranging up to 60% of the volume in a few examples (Fig. 7c). 22 sets of microthermometric data were successfully obtained in this study. The T_mCO_2 (°C) varies from −60.6 to −57.3 °C, which indicates the presence of other components in the fluids in addition to CO_2. Melting temperatures of clathrate vary from 5.6 to 9.3 °C, giving salinities from 1.42 to 8.03 wt%, NaCl equiv. The total homogenization temperatures of the fluid inclusions vary from 233.1 to 346.2 °C (average 288.1 °C).

6.4. δ^{18}O and δD values of quartz and fluids

Oxygen isotopes of quartz from gold-bearing quartz veins show a narrow range between 17.3 and 19.2‰. Using the minimum trapping temperature that is defined by the average homogenized temperatures of the fluid inclusions (i.e. 288.1 °C), we calculated δ^{18}O values of fluids that range from 9.96 to 11.86‰ (Table 3). Fluid inclusions from quartz samples have δD values ranging from −75 to −97.1‰ (Table 3).

Table 2
In-situ Pb isotopic compositions of sulfides from the North Kostobe gold deposit.

Analysis_ID	Mineral	$^{206}Pb/^{204}Pb$	1σ	$^{208}Pb/^{204}Pb$	1σ	$^{207}Pb/^{204}Pb$	1σ
K051-02	Aspy	18.195	0.023	37.773	0.048	15.460	0.019
K051-03	Aspy	18.133	0.038	37.792	0.079	15.498	0.032
K051-04	Aspy	18.019	0.015	37.572	0.031	15.425	0.012
K051-06	Aspy	18.130	0.019	37.640	0.038	15.443	0.015
K051-10	Aspy	18.218	0.009	37.603	0.018	15.418	0.007
K05-9-01	Aspy	17.800	0.080	37.268	0.170	15.321	0.069
K05-9-02	Aspy	17.954	0.082	37.515	0.172	15.428	0.071
K05-9-03	Aspy	17.969	0.021	37.624	0.045	15.463	0.018
K05-9-04	Aspy	17.902	0.121	37.429	0.248	15.381	0.101
K051-12	Aspy	18.029	0.007	37.687	0.015	15.466	0.006
K051-13	Aspy	17.965	0.003	37.647	0.007	15.468	0.003
K19-01	Aspy	18.229	0.052	37.980	0.113	15.545	0.046
K19-02	Aspy	18.299	0.048	38.063	0.099	15.589	0.042
K091-02	Aspy	19.190	0.028	38.130	0.054	15.519	0.022
K091-04	Aspy	19.346	0.047	38.103	0.092	15.457	0.037
K091-01	Py2	17.978	0.005	37.564	0.010	15.451	0.004
K051-11	Py2	17.976	0.002	37.647	0.005	15.464	0.002
K051-14	Py2	17.988	0.005	37.689	0.010	15.471	0.004
K051-15	Py2	18.040	0.008	37.727	0.015	15.488	0.006
K091-03	Py2	19.249	0.028	38.243	0.042	15.512	0.016
K091-01	Py2	17.978	0.005	37.564	0.010	15.451	0.004
K073-08	Py2	17.951	0.004	37.641	0.008	15.463	0.003
K072-01	Py2	18.331	0.049	38.031	0.097	15.554	0.039
K072-02	Py2	18.011	0.005	37.685	0.009	15.461	0.004
K072-03	Py2	17.978	0.012	37.638	0.024	15.456	0.010
K092-1	Py2	18.107	0.037	37.765	0.078	15.506	0.032
K092-2	Py2	17.989	0.018	37.556	0.037	15.419	0.015
K092-3	Py2	18.192	0.019	37.798	0.036	15.452	0.016
K051-01	Py2	18.198	0.013	37.802	0.025	15.484	0.010
K051-05	Py2	18.137	0.025	37.809	0.052	15.517	0.021
K051-07	Py2	18.116	0.021	37.845	0.044	15.495	0.016
K051-09	Py2	17.989	0.022	37.653	0.047	15.467	0.019
K073-02	Py2	17.986	0.003	37.666	0.006	15.464	0.003
K073-04	Py2	18.010	0.007	37.714	0.016	15.483	0.006
K073-06	Py2	18.015	0.010	37.671	0.019	15.466	0.008
K19-03	Py2	18.036	0.015	37.724	0.030	15.477	0.012
K19-05	Py2	18.082	0.030	37.741	0.063	15.465	0.026
K051-08	Py1	18.118	0.039	37.600	0.079	15.443	0.032
K073-01	Py1	17.996	0.002	37.698	0.004	15.476	0.001
K073-03	Py1	17.987	0.002	37.685	0.003	15.474	0.001
K073-05	Py1	17.996	0.002	37.702	0.004	15.479	0.001
K19-04	Py1	17.965	0.002	37.680	0.005	15.480	0.002
K19-06	Py1	17.956	0.001	37.683	0.003	15.485	0.001
K072-04	Py1	17.994	0.008	37.715	0.017	15.484	0.007
K072-05	Py1	17.954	0.004	37.664	0.008	15.468	0.003
K072-06	Py1	17.944	0.005	37.632	0.010	15.461	0.004
Standard	NIST 610						
20150411A55		17.051	0.001	36.981	0.003	15.514	0.001
20150411A56		17.049	0.001	36.980	0.004	15.514	0.001
20150411A67		17.050	0.001	36.977	0.004	15.513	0.001
20150411A68		17.054	0.002	36.994	0.004	15.519	0.002
20150411A75		17.055	0.001	36.983	0.003	15.519	0.001
20150411A76		17.055	0.001	36.984	0.003	15.519	0.001
20150411A77		17.055	0.002	36.987	0.004	15.517	0.002
20150411A78		17.057	0.002	36.987	0.004	15.517	0.002
20150411A80		17.053	0.002	36.982	0.005	15.516	0.002
20150411A81		17.053	0.002	36.979	0.004	15.514	0.001
20150411A95		17.048	0.001	36.973	0.003	15.511	0.001
20150411A97		17.045	0.001	36.965	0.003	15.507	0.001
20150411A109		17.054	0.001	36.982	0.003	15.516	0.001

Aspy: arsenopyrite; Py: pyrite.

7. Discussion

The North Kostobe gold deposit formed in a deformed terrane within an accretionary orogen. Gold mineralization is hosted in dilational shear zones linked to regional faults, and the geometry of the orebody is structurally controlled. Gold is associated with arsenopyrite and pyrite in metasedimentary rocks, and quartz in the auriferous quartz-carbonate veins contains abundant low-salinity CO_2-bearing fluid inclusions. These features indicate that the North Kostobe gold deposit are comparable to the orogenic style gold deposits defined by Groves et al. (1998, 2003) and Goldfarb et al. (2005).

7.1. Origin of ore-forming fluids

7.1.1. Source of fluids

The auriferous quartz-carbonate veins in the North Kostobe gold deposit have δD values (−75 to −96.5‰) overlapping with those of lode gold deposits worldwide (−20 to −80‰) (Fig. 8) (Kerrich, 1987;

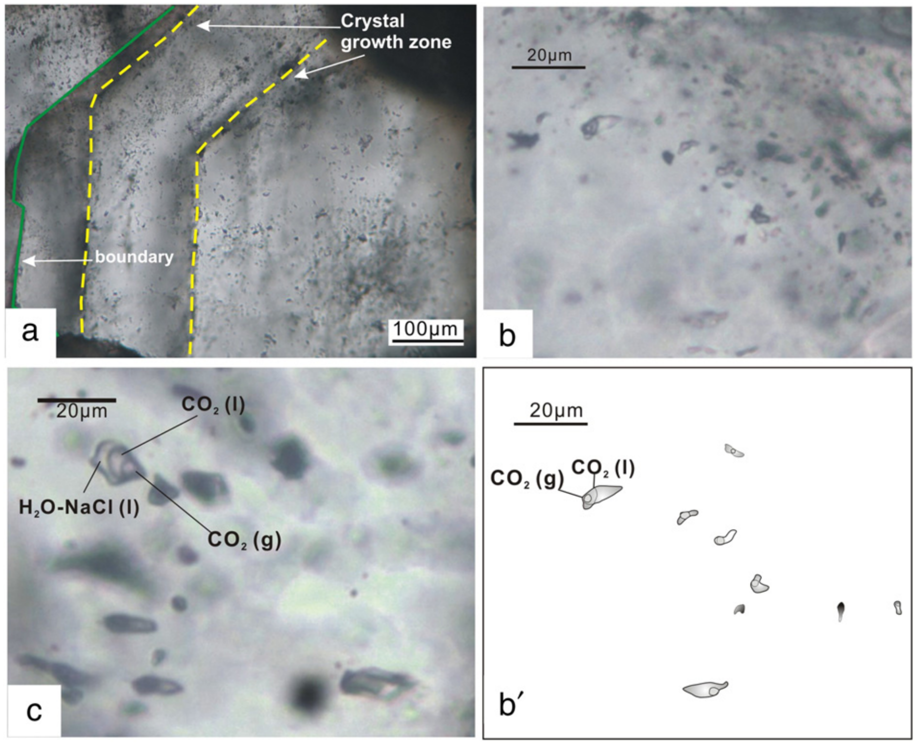

Fig. 7. Representative photos of fluid inclusions in gold-bearing quartz vein samples. a. growth zone in single dusty quartz crystals; b. pseudo-secondary cluster of fluid inclusions; (b') a sketches version of the same; c. three phases CO_2-H_2O fluid inclusions.

Table 3
Oxygen and hydrogen isotopic compositions of quartz from auriferous quartz-carbonate veins in the North Kostobe gold deposit.

Samples	δD_{vsmow}‰	$\delta^{18}O_{vsmow}$‰	Average T_{tot}(°C)	$\delta^{18}O_{H2O}$‰
07-61.5	−82.8	17.3	288.1	9.96
07-69.9	−96.5	18.8	288.1	11.46
05-90.2	−75	18	288.1	10.66
09-81.4	−97.1	19.2	288.1	11.86
19-96.9	−92.8	18.4	288.1	11.06

McCuaig and Kerrich, 1998; Ridley and Diamond, 2000) and that of the Juneau gold belt in Alaska (Goldfarb et al., 1991). The low δD values (<−80‰) can be the result of reaction between deep-sourced non-meteoric (metamorphic) fluids and δD-depleted organic matter in host rocks (e.g., some carbonaceous turbidite-hosted lode gold deposits; Goldfarb et al., 1989; McCuaig and Kerrich, 1998; Jia et al., 2001) or due to the exchange effect with CH_4-rich reduced fluids (Craw, 2002). However, some authors have also suggested that the low δD values may reflect a mixed signature of several generations of secondary fluid inclusions that are incorporated into primary fluids due to bulk extraction measurement of δD values (e.g. Goldfarb et al., 1991; McCuaig

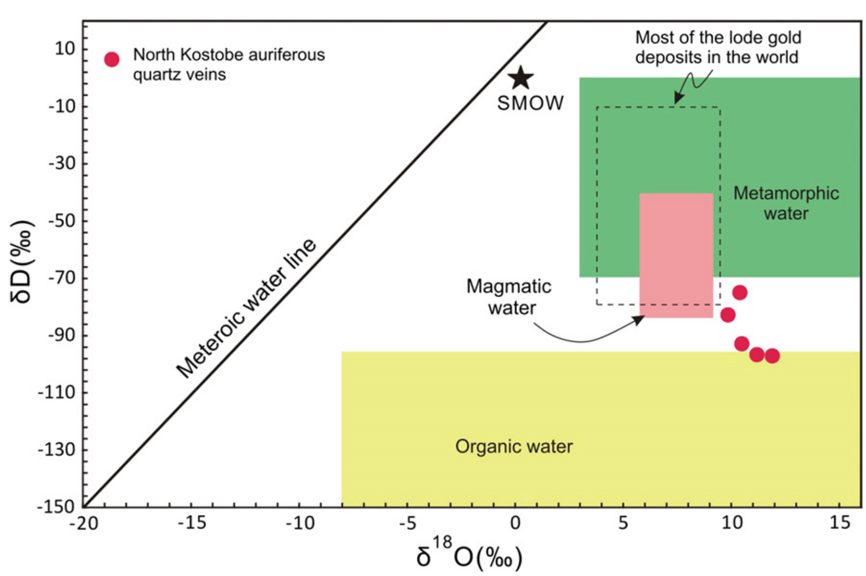

Fig. 8. Plot of δD vs. $\delta^{18}O_{H2O}$ for the ore-forming fluids of the North Kostobe gold deposit. Fields of magmatic water, metamorphic water and organic water are after Sheppard (1986).

and Kerrich, 1998). It is notable that the δD values of modern meteoric water in northeastern Kazakhstan range from −100 to −120‰ (Pourcelot et al., 2014), the same as for organic waters. As such, consequently distinguishing contributions from organic water versus meteoric water based on measured δD values is not possible. However, the narrow range of the measured $\delta^{18}O_{H2O}$ values (9.96 to 11.86‰), which are comparable to most gold lodes deposits worldwide (5 to 16‰) (Bierlein and Crowe, 2000; Jia et al., 2003), fits well with the $\delta^{18}O_{H2O}$ values for metamorphic water and are far from local meteoric water values. Such heavy $\delta^{18}O_{H2O}$ values were interpreted to be reflecting $\delta^{18}O$-enriched metasedimentary rocks (e.g. Chen et al., 2002; Ding et al., 2014; Kerrich and Feng, 1992). Other potential oxygen sources are not available due to the tight clustering of $\delta^{18}O_{H2O}$ values. Therefore, we suggest that the $\delta^{18}O_{H2O}$ and δD values of the ore-fluids are most likely indicative of metamorphic fluids originated at deeper levels of the crust (Goldfarb et al., 2005), through dehydration of $\delta^{18}O$-enriched metasedimentary rocks during metamorphism.

7.1.2. Source of sulfur

The py1 grains have $\delta^{34}S$ values (−4.5 to +2.6‰) (Fig. 9a) similar to the py2 and arsenopyrite of the second generation (−6 to +1.9‰) (Fig. 9b), suggesting that both generations may have a common sulfur source or the sulfur of the second generation was sourced from the py1 grains. Such a range of $\delta^{34}S$ values is comparable to most orogenic lode gold deposits in the world ($\delta^{34}S$ = 0–9‰, Groves et al., 1998; McCuaig and Kerrich, 1998). Although near-zero $\delta^{34}S$ values are traditionally interpreted to be of magmatic origin (Hoefs, 1997), the range of the $\delta^{34}S$ values (−6 to +2.6‰) does not support a homogeneous magmatic sulfur source. Indeed, the $\delta^{34}S$ values of the second generation sulfides of the North Kostobe gold deposit are similar to many sediment-hosted gold deposits of which the $\delta^{34}S$ values vary with the age of host terranes (e.g., Chang et al., 2008). Furthermore, the $\delta^{34}S$ values of this deposit are comparable with other gold deposits in the Kalba gold province ($\delta^{34}S$ = −10.2 to 0.5‰, Table 4) and the relatively more $\delta^{34}S$–depleted values (Table 4) while consistent with an involvement of crustal sulfur. As such, we propose that the sulfur of the North Kostobe gold deposit was likely mainly sourced from the sedimentary rocks in the hosting terrane.

Py3 in micro-fractures has a bimodal distribution and large spread in $\delta^{34}S$ values from −40 to +54.5‰ (Fig. 9c). Such an extreme variations of $\delta^{34}S$ values in a single sample (Fig. 6i) can only be attributed to sulfur-reducing bacterial (SRB) activity (Canfield, 2001; Seal, 2006). Indeed, bacterial SO_4^{2-} reduction can usually cause a fractionation with ~20 to 40‰ differences in terms of $\delta^{34}S$ values (Canfield, 2001). The extremely positive $\delta^{34}S$ values are likely caused by a Rayleigh fractionation process in a closed system in which the SO_4^{2-} consumed by bacterial activity is not replaced. Based on the occurrence and the $\delta^{34}S$ values of py3, the only reasonable explanation is that py3 is not related to the ore-forming fluids since sulfur reducing bacteria usually survive between 0 and 110 °C (Seal, 2006), much below the temperature of the hydrothermal environment forming the former generations of sulfides.

7.1.3. Source of lead

Both the first and second generations of sulfides have similar ranges of Pb isotopic ratios (Fig. 10), suggesting a common source of lead for them. Such a broad variation of the Pb isotopic signature cannot be produced by radiogenic decay of U or Th since the formation of the deposit at ~285 Ma, because the plots do not show a good correlation. Moreover, it is expected that radiogenic decay of even small amounts of U or Th in Pb-poor minerals like pyrite would significantly increase the Pb isotopic ratios for an age of ~285 Ma (e.g., Chiaradia et al., 2006). The isotopic compositions of three samples with distinctly higher $^{206}Pb/^{204}Pb$ values (Fig. 10) have probably formed in this way. Excluding the three samples, the remaining analyses with a broad range of Pb isotopic ratios likely indicates contributions of Pb from multiple sources. The steep trend defined by the uranogenic Pb isotopic compositions (Fig. 10b) suggests mixing between more radiogenic Pb source (e.g. orogeny Pb) and less radiogenic Pb source (e.g. mantle, lower crust Pb).

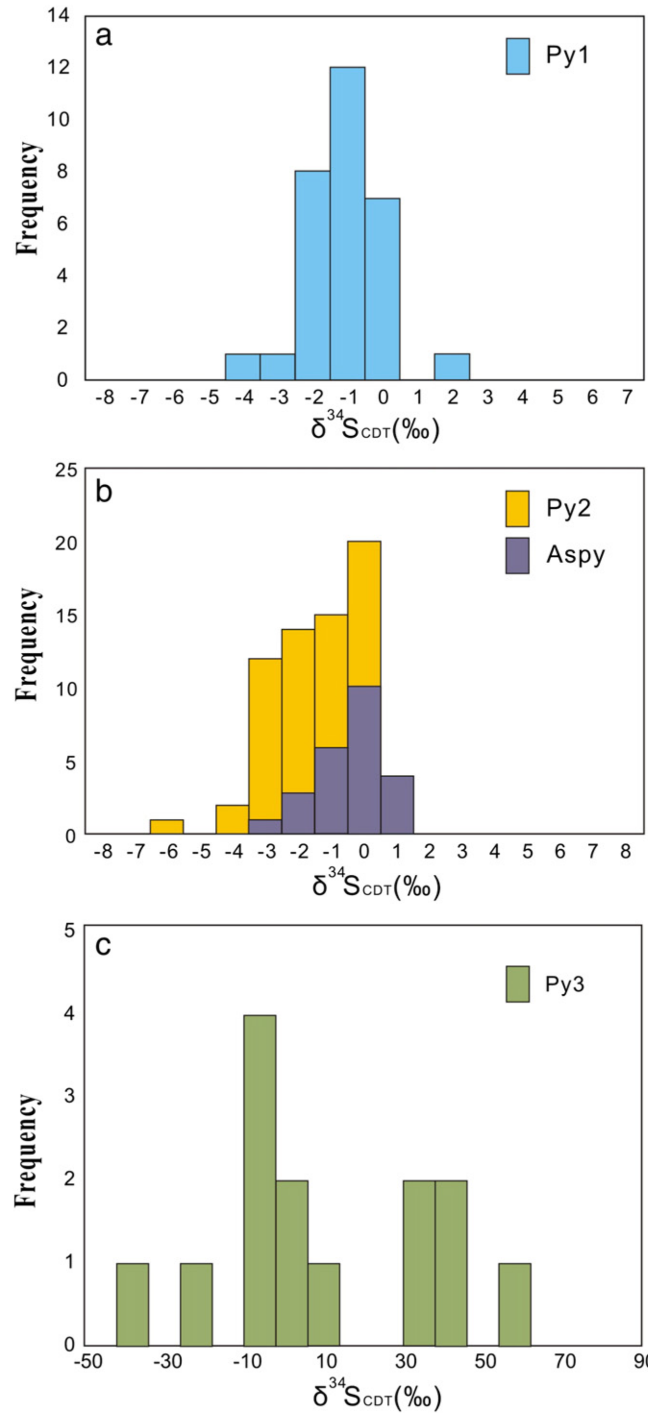

Fig. 9. Histogram of $\delta^{34}S$ values for different generations of sulfides in the North Kostobe gold deposit, a. Py1; b. Py2 and arsenopyrite; and c. fracture-filled py3 which shows extreme variation of $\delta^{34}S$ values.

The mantle-Pb affinity could be attributed to syn/post-tectonic magmatic activities (e.g., hidden plutons) during the convergence of the Kazakhstan-Siberia continental margins. Moreover, the spread of Pb isotopic compositions from ore minerals in the North Kostobe deposit are similar to those ore deposits in Chinese Altay presented in Chiaradia et al. (2006). Considering that part of the Chara shear zone

Table. 4
Summary of sulfur isotopic compositions of sulfides from gold deposits in the Kalba gold province.

Deposit	Mineral	δ^{34}S ‰	No. of analysis	References
Suzdal	Pyrite	0, 0.5	2	Kovalev et al. (2009)
	Arsenopyrite	−1.8	1	Kovalev et al. (2009)
	Pyrite	−10.2 to 0	7	Kovalev et al. (2011)
	Arsenopyrite	−7.6, −1.2	2	Kovalev et al. (2011)
	Stibnite	−4.9 to 0.7	4	Kovalev et al. (2011, 2014)
Zherek	Arsenopyrite	−3.2	1	Kovalev et al. (2011, 2014)
Bolshevik	Arsenopyrite	−2.4, −1.3	2	Kovalev et al. (2011)
	Pyrite	−0.7, −0.3	2	Kovalev et al. (2011)

extends to the Chinese Altay, it is plausible that the Chara shear zone in Kazakhstan segment shares the same Pb reservoir with that in the Chinese Altay. We also speculate that the host sedimentary country rocks are likely one of the potential Pb sources for the Pb in sulfides since host rocks Pb source for Phanerozoic sediment-hosted orogenic gold deposits has also been reported in a number of studies (e.g. Chen et al., 2012; Ding et al., 2014; Wang et al., 2015; Liu et al., 2015).

7.1.4. Implications for the source of gold

Pyritic carbonaceous metasedimentary rocks have long been suggested to be a viable source rocks for orogenic gold deposits (Tomkins, 2010; Gaboury, 2013; Pitcairn et al., 2006, 2015; Zhong et al., 2015). Both gold and sulfur can be released from sedimentary/diagenetic pyrite during conversion from pyrite to pyrrhotite during metamorphism and subsequently entered into the metamorphic fluids. In our cases, the new Pb-S-O-H isotopic data from the North Kostobe gold deposit allow us to propose that the hosting sedimentary terrane could be also the source for gold (c.f. Large et al., 2011, 2015).

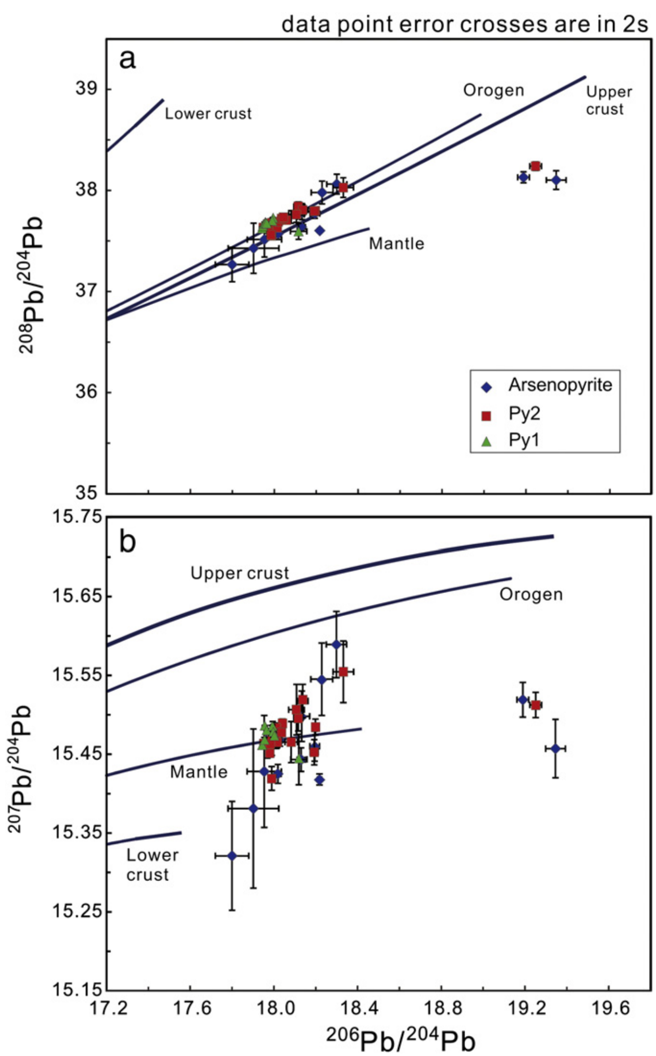

Fig. 10. Conventional thorogenic (a) and uranogenic (b) Pb compositions plots of py1, py2 and arsenopyrite. The evolution lines for lower crust, mantle and upper crust are from Zartman and Haines (1988).

7.2. A genetic model for the North Kostobe deposit

Formation of gold deposits in the Bakyrchik ore district was once summarized by Daukeev et al. (2004) and was thought to involve three stages: (1) initial gold concentration in the basin during diagenesis; (2) local remobilization of gold within mesozonal-epizonal crustal levels (2 to 6 km) during regional metamorphism; and (3) thermal-

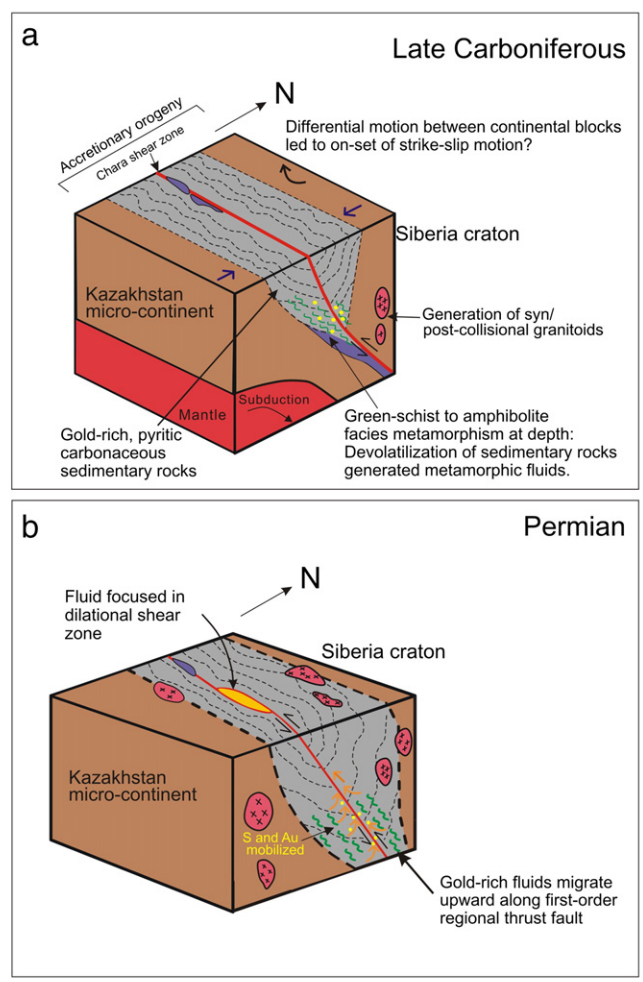

Fig. 11. A genetic model of the North Kostobe gold deposit. See text for detailed explanation.

driven remobilization of previously formed gold and its re-deposition in geochemical barriers. The model implies a local redistribution of gold in the basin into structural/chemical traps which led to mineralization. However, this model is not supported by our new data suggesting that the ore forming fluid and gold were originated from deeper parts of the crust (15 to 20 km).

Here, we propose a new genetic model for the North Kostobe gold deposit. Gold was sourced from erosion of continental rocks and pre-existing gold province and entered the sedimentary basin where Au-rich sedimentary/diagenetic pyrite has formed (c.f. Large et al., 2011, 2015). During the orogenic stage (Fig. 11) in the late Carboniferous, convergence and accretion between the Kazakhstan and Siberia continents caused extensive crustal thickening, compression, and deformation in the fore-arc region along the plate margin, resulting in deformation and metamorphism of the whole sequence of fore-arc sedimentary rocks. Metamorphic fluids were predominantly derived from the dehydration of ^{18}O–enriched metasedimentary rocks during prograde metamorphism. Meanwhile, gold, sulfur and other trace elements from the Au-rich sedimentary source rocks were leached by fluids produced and transported into zones of weakness.

The collision between the Kazakhstan microcontinent and the Siberian craton has also produced a series of NW–SE trending regional faults that played an important role in fluid flow and ore deposition. The onset of strike-slip motion in the Chara shear zone in the Permian, which was coeval with the Irtysh shear zone, may have led to the opening of E-W dilational shear zones along the regional strike slip faults. Ore-forming fluids migrated upward from deeper crust through regional structure and channeled to dilational shear zones where gold was deposited.

7.3. Implications for regional exploration

The recognition of the North Kostobe gold deposit as a typical orogenic gold deposit has important implications for the metallogeny of the region. Although Pb isotopic compositions in gold-bearing sulfides suggest that there might be hidden plutons in the region, these intrusions are not essentially responsible for gold mineralization (Goldfarb et al., 2001). For example, the deposit does not show typical geological characteristics of intrusion-related gold system such as sheeted veins, diverse mineralization styles, or metal zoning (e.g. Thompson et al., 1999; Goldfarb et al., 2005; Hart and Goldfarb, 2005; Hart, 2007). An exploration model for orogenic gold deposits should be applied, which primarily targets structural traps along the regional crustal scale structures showing structural complexity, such as dilational jogs and change in strike along regional faults which possibly host mineralization (Groves et al., 2000). Although carbonate, biotite and sericite alterations are recognized in the deposit, the development of alteration around the veins is usually restricted because of low permeability of the host strata.

The Kalba gold province in eastern Kazakhstan is a relatively unexplored gold province where mining activities in the past mostly targeted visible gold in quartz reef and near surface oxidized ore zones. A significant amount of primary sulfide mineralization may still remain at depth. Moreover, the North Kostobe gold deposit shares many similar features with the Muruntau gold deposit in the Southern Tianshan orogenic belt, including tectonic setting, host rocks, ore mineralogy, stable isotope signature, and fluid characteristics (e.g. Berger et al., 1994; Graupner et al., 2001; Wilde et al., 2001). As a relatively unexploited region compared to the Southern Tianshan orogenic belt, there is a great potential to discover more Muruntau-like or even Muruntau scale gold deposits in the future.

8. Conclusions

Based on the geology, mineralogy, fluid inclusions, H-O isotope data, and in-situ S-Pb data, the following conclusions concerning on the origin of the North Kostobe gold deposit in eastern Kazakhstan can be drawn:

1. The ore-forming fluids of the North Kostobe gold deposit are CO_2-rich with low salinity and are metamorphic in origin.
2. The sulfur of the major Au mineralization was mainly sourced from pyritic carbonaceous sedimentary rocks. The late stage pyrite veins with extreme sulfur isotope values are best explained by biological activity without genetic relationships to the Au mineralization.
3. Lead in sulfides was derived from a mixed Pb sources.
4. The North Kostobe gold deposit is comparable to typical orogenic gold deposits. Such recognition has important implications for exploration of similar type deposits in the Kalba gold province.

Acknowledgements

International Resources Group, Kazakhstan Ltd. are thanked for arranging logistics and sampling in the field. The research is supported by the “Thousand Youth Talents Plan” grant (Y6CR0610000) to Wei Terry Chen and a research grant from State Key Laboratory for Mineral Deposits Research (20-15-01). Additional support was provided by the CAS/SAFEA International Partnership Program for Creative Research Teams-Intraplate Mineralization Research Team (KZZDEW-TZ-20). This is a Finnish Geosciences Research Laboratory (SGL) contribution. Liu Zerui and Yang Shenghong are thanked for their assistance with in-situ Pb and S isotopic analyses. Reimar Seltmann, Massimo Chiaradia and an anonymous reviewer are also thanked for the constructive comments and criticism to greatly improve this manuscript.

Appendix A. Supplementary data

Supplementary data to this article can be found online at http://dx.doi.org/10.1016/j.oregeorev.2016.10.004.

References

Berger, B.R., Drew, L.J., Goldfarb, R.J., Snee, L.W., 1994. An epoch of gold riches: the late Paleozoic in Uzbekistan, Central Asia. SEG Newsletter 16, 1–11.

Berzin, N.A., Coleman, R.G., Dobretsov, N.L., Zonenshain, L.P., Xiao, X., Chan, E.Z., 1994. Geodynamic map of the Western part of Paleoasian Ocean. Russ. Geol. Geophys. 35, 1–5.

Bierlein, F.P., Crowe, D.E., 2000. Phanerozoic orogenic lode gold deposits. In: Hagemann, S.G., Brown, P.E. (Eds.), Gold in 2000. Rev. Econ. Geol. Vol. 13, pp. 103–139.

Buslov, M.M., Saphonova, I.Y., Watanabe, T., 2001. Evolution of the Paleo-Asian Ocean (Altai–Sayan region, Central Asia) and collision of possible Gondwana-derived terranes with the southern marginal part of the Siberian continent. Geosci. J. 5, 203–224.

Buslov, M.M., Watanabe, T., Smirnova, L.V., Fujiwara, I., Iwata, K., de Grave, J., Semakov, N.N., Travin, A.V., Kir'yanova, A.P., Kokh, D.A., 2003. Role of strike-slip faulting in Late Paleozoic–Early Mesozoic tectonics and geodynamics of the Altai-Sayan and East Kazakhstan regions. Russ. Geol. Geophys. 44, 47–72.

Buslov, M.M., Watanabe, T., Fujiwara, Y., Iwata, K., Smirnova, L.V., Safonova, I.Y., Semakov, N.N., Kiryanova, A.P., 2004. Late Paleozoic faults of the Altai region, Central Asia: tectonic pattern and model of formation. J. Asian Earth Sci. 23, 655–671.

Canfield, B.E., 2001. Biogeochemistry of sulphur isotopes. Rev. Mineral. Geochem. 43, 607–636.

Chang, Z., Large, R.R., Maslennikov, V., 2008. Sulfur isotopes in sediment-hosted orogenic gold deposits: evidence for an early timing and a seawater sulfur source. Geology 36, 971–974.

Chen, H.Y., Chen, Y.J., Baker, M., 2012. Isotopic geochemistry of the Sawayaerdun orogenic-type gold deposit, Tianshan, northwest China: implications for ore genesis and mineral exploration. Chem. Geol. 310–311.

Chen, K., Yuan, H., Bao, Z., Zong, C., Dai, M., 2013. Precise and accurate in situ determination of lead isotope ratios in NIST, USGS, MPI-DING and CGSG glass reference materials using femtosecond laser ablation MC-ICP-MS. Geostandards and Geo-analytical Research, http://dx.doi.org/10.1111/j.1751-908X.2013.00223.x.

Chiaradia, M., Konopclko, D., Seltmann, R., Cliff, R.A., 2006. Lead isotope variations across terrane boundaries of the Tien Shan and Chinese Altay. Mineral. Deposita 41, 411–428.

Clayton, R.N., Mayeda, T.K., 1963. The use of bromine pentafluoride in the extraction of oxygen from oxides and silicates for isotopic analysis. Geochim. Cosmochim. Acta 27, 43–52.

Clayton, R.N., O'Neil, J.R., Mayeda, T.K., 1972. Oxygen isotope exchange between, quartz and water. Journal of Geophysics Reviews 77, 3057–3067.

Colemen, M.L., Shepherd, T.J., Durham, J.J., Rouse, J.E., Moore, G.R., 1982. Reduction of water with zinc for hydrogen isotope analysis. Anal. Chem. 54, 993–995.

Craw, D., 2002. Geochemistry of late metamorphic hydrothermal alteration and graphitisation of host rock, Macraes gold mine, Otago Schist, New Zealand. Chem. Geol. 191, 257–275.

Daukeev, S.Z., Uzhkenov, B.S., Bespaev, Kh.A., Miroshnichenko, L.A., Mazurov, A.K., Sayduakasov, M.A. (Eds.), 2004. Atlas of Mineral Deposit Models. Printing House "Center for Geoinformation of the MF RK", Almaty.

Daukeev, S.Z., Kim, B.C., Li, T., Petrov, O.V., Tomurtogoo, O., 2008. Atlas of Geological Maps of Central Asia and Adjacent Areas. Geological Publishing House, Beijing.

Didenko, A.N., Mossakovskiy, A.A., Pecherskiy, D.M., Ruzhentsev, S.G., Samygin, S.G., Kheraskova, T.N., 1994. Geodynamics of Paleozoic Oceans of Central Asia Russian Geology and Geophysics. Vol. 35 pp. 48–62.

Ding, Q.F., Wu, C.Z., Santosh, M., Fu, Y., Dong, L.H., Qu, X., Gu, L.X., 2014. H-O, S and Pb isotope geochemistry of the Awanda gold deposit in southern Tianshan, Central Asian orogenic belt: implications for fluid regime and metallogeny. Ore Geol. Rev. 62, 40–53.

Gaboury, D., 2013. Does gold in orogenic deposits come from pyrite in deeply buried carbon-rich sediments? Insight from volatiles in fluid inclusions. Geology 41, 1207–1210.

Gilbert, S.E., Danyushevsky, L.V., Rodermann, T., Shimizu, A., Gurenko, A., Meffre, S., Thomas, H., Large, R.R., Death, D., 2014. Optimisation of laser parameters for the analysis of sulphur isotopes in sulphide minerals by laser ablation ICP-MS. J. Anal. At. Spectrom. 29, 1042–1051.

Glorie, S., Grave, J.D., Delvaus, D., Buslov, M.M., Zhimulev, F.I., Vanhaecke, F., Elburg, M.A., Van den haute, P., 2012. Tectonic history of the Irtysh shear zone (NE Kazakhstan): new constraints from zircon U/Pb dating, apatite fission track dating and paleostress analysis. J. Asian Earth Sci. 45, 138–149.

Goldbridges Golbal Resouces Plc, 2014. JORC Resource and Reserve Estimate. (Retrieved from) http://www.goldbridgesplc.com/operations/sekisovskoye.html#jorc-re-source-estimate.

Goldfarb, R.J., Leach, D.L., Rose, S.C., Landis, G.P., 1989. Fluid inclusion geochemistry of gold-bearing quartz veins of the Juneau gold belt, southeastern Alaska: implications for ore genesis. Econ. Geol. Monogr. 6, 363–375.

Goldfarb, R.J., Newberry, R.J., Pickthorn, W.J., Gent, C.A., 1991. Oxygen, hydrogen and sulfur isotope studies in the Juneau gold belt, southeastern Alaska: constraints on the origin of hydrothermal fluids. Econ. Geol. 86, 66–80.

Goldfarb, R.J., Groves, D.I., Gardoll, S., 2001. Orogenic gold and geologic time: a global synthesis. Ore Geol. Rev. 18, 1–75.

Goldfarb, R.J., Baker, T., Dube, B., Groves, D.J., Hart, C.J.R., Gosselin, P., 2005. Distribution, Character, and Genesis of Gold Deposits in Metamorphic Terranes. Economic Geology 100th Anniversary Volume. pp. 407–450.

Goldfarb, R.J., Taylor, R.D., Collins, G.S., Goryachev, N.A., Orlandini, O.F., 2014. Phanerozoic continental growth and gold metallogeny of Asia. Gondwana Res. 25, 48–102.

Gosselin, P., Dubé, B., 2005. Gold deposits of the world: distribution, geological parameters and gold content. Geological Survey of Canada, Open file 4895.

Graupner, T., Kempe, U., Spooner, E.T.C., Bray, C.J., Kremenetsky, A.A., Irmer, G., 2001. Microthermometric, laser Raman spectroscopic, and volatile/ion chromatographic analysis of hydrothermal fluids in the Paleozoic Muruntau Au-quartz vein ore field, Uzbekistan. Econ. Geol. 96, 1–23.

Groves, D.I., Goldfarb, R.J., Gebre-Mariam, M., Hagemann, S.G., Robert, F., 1998. Orogenic gold deposits: a proposed classification in the context of their crustal distribution and relationship to other gold deposit types. Ore Geol. Rev. 13, 7–27.

Groves, D.I., Goldfarb, R.J., Knox-Robinson, C.M., Ojala, J., Gardoll, S., Yun, G., Holyland, P., 2000. Late-kinematic timing of orogenic gold deposits and its significance for computer-based exploration techniques with emphasis on the Yilgarn block, Western Australia. Ore Geol. Rev. 17, 1–38.

Groves, D.I., Goldfarb, R.J., Robert, F., Hart, C.J.R., 2003. Gold deposits in metamorphic belts: overview of current understanding, outstanding problems, future research, and exploration significance. Econ. Geol. 98, 1–29.

Hart, C.J.R., 2007. Reduced intrusion-related gold systems. In: Goodfellow, W.D. (Ed.), Mineral Deposits of Canada: A Synthesis of Major Deposit Types, District Metallogeny, the Evolution of Geological Provinces and Exploration Methods Vol. No. 5. Geological Association of Canada, Mineral Deposits Division, Special Publication, pp. 95–112.

Hart, C.J.R., Goldfarb, R.J., 2005. Distinguishing intrusion-related from orogenic gold systems. Proceedings of the 2005 New Zealand Minerals Conference, Auckland, New Zealand, pp. 125–133 13–16 November.

Hoefs, J., 1997. Stable Isotope Geochemistry. 3rd Edition. Springer-Verlag, Berlin 201 pp.

Iwata, K., Obut, O.T., Buslov, M.M., 1997. Devonian and lower carboniferous radiolarian from the chara ophiolite belt, East Kazakhstan. Micropaleontologist 10, 27–32.

Jia, Y., Li, X., Kerrich, R., 2001. Stable isotope (O, H, S, C and N) systematics of quartz vein systems in the tubidite-hosted Central and North Deborah gold deposits of the Bendigo gold field, Central Victoria, Australia: constraints on the origin of ore forming fluids. Econ. Geol. 96, 705–721.

Jia, Y., Kerrich, R., Goldfarb, R., 2003. Metamorphic origin of ore-forming fluids for orogenic gold-bearing quartz vein systems in the North America Cordillera: constraint from a reconnaissance study of δ^{15}N, δD and δ^{18}O. Econ. Geol. 98, 109–123.

Jochum, K.P., Stall, B., 2008. Reference materials for elemental and isotopic analyses by LA-(MC)-ICP-MS: successes and outstanding needs. In: Sylvester, P. (Ed.), Laser Ablation ICP-MS in the Earth Sciences: Current Practices and Outstanding Issues. Mineralogical Association of Canada (Vancouver, BC), pp. 147–168.

Kalinin, Y.A., Kovalev, K.R., Naumov, E.A., Kirillov, M.V., 2009. Gold in weathering crust at the Suzdal' deposit (Kazakhstan). Russ. Geol. Geophys. 50, 174–187.

Kerrich, R., 1987. The Stable Isotope Geochemistry of Au-Ag Vein Deposits in Metamorphic Rocks: Mineralogical Association of Canada short course handbook. v.13, 287–336.

Kerrich, R., Feng, R., 1992. Archean geodynamics and the Abitibi–Pontiac collision: implications for advection of fluids at transpressive collisional boundaries and the origin of giant quartz vein systems. Earth Sci. Rev. 32, 33–60.

Kovalev, K.R., Kalinin, Y.A., Naumov, E.A., Pirajno, F., Borisenko, A.S., 2009. A mineralogical study of the Suzdal sediment hosted gold deposit, Eastern Kazakhstan: implications for ore genesis. Ore Geol. Rev. 35, 186–205.

Kovalev, K.R., Kalinin, Y.A., Naumov, E.A., Kolesnikova, M.K., Korolyuk, V.N., 2011. Gold-bearing arsenopyrite in eastern Kazakhstan gold-sulfide deposits. Russ. Geol. Geophys. 52, 178–192.

Kovalev, K.R., Kalinin, Y.A., Naumov, E.A., Myagkaya, M.K., 2014. Relationship of antimony with gold mineralization in the ore districts of Eastern Kazakhstan. Russ. Geol. Geophys. 55, 1170–1182.

Kuz'mina, O.N., D'yachkov, B.A., Vladimirov, A.G., Kirillov, M.V., Redin, Y.O., 2013. Geology and mineralogy of East Kazakhstan gold bearing jasperoids. Russ. Geol. Geophys. 54, 1471–1483.

Large, R.R., Maslennikov, V.V., Robert, F., Danyushevsky, L., Chang, Z., 2007. Multistage sedimentary and metamorphic origin of pyrite and gold in the giant Sukhoi log deposit, Lena gold province, Russia. Econ. Geol. 102, 1233–1267.

Large, R.R., Bull, S.W., Maslennikov, V., 2011. A carbonaceous sedimentary source-rock model for Carlin-type and orogenic gold deposits. Econ. Geol. 106, 331–358.

Large, R.R., Gregory, D.D., Steadman, J.A., Tomkins, A.G., Lounejeva, E., Danyushevsky, L.V., Halpin, J.A., Maslennikov, V., Sack, P.J., Mukherjee, I., Berry, R., Hickman, A., 2015. Gold in the oceans through time. Earth Planet. Sci. Lett. 428, 139–150.

Li, D., He, D., Ma, D., Tang, Y., Kong, Y., Tang, J., 2015a. Carboniferous–Permian tectonic framework and its later modifications to the area from eastern Kazakhstan to southern Altai: insights from the Zaysan–Jimunai Basin evolution. J. Asian Earth Sci. 113, 16–35.

Li, P., Sun, M., Rosenbaum, G., Cai, K., Yu, Y., 2015b. Structural evolution of the Irtysh shear zone (northwestern China) and implications for the amalgamation of arc systems in the Central Asian Orogenic Belt. J. Struct. Geol. http://dx.doi.org/10.1016/j.jsg.2015.08.008.

Liu, J., Liu, C., Carranza, E.J.M., Li, Y., Mao, Z., Wang, J., Wang, Y., Zhang, J., Zhao, D., Zhang, H., Shan, L., Zhu, L., Lu, R., 2015. Geological characteristics and ore-forming process of the gold deposits in the western Qinling region, China. J. Asian Earth Sci. 103, 40–69.

Ludwig, K.R., 2008. Isoplot/Ex Version 3.7, a Geochronological Toolkit for Microsoft Excel. Berkeley Geochronology Center, Berkeley, CA, USA.

Lyons, J.J., Coe, R.S., Zhao, X., Renne, P.R., Kazansky, A.Y., Izokh, A.E., Kungurtsev, L.V., Mitrokhin, D.V., 2002. Paleomagnetism of the early Triassic Semeitau igneous series, eastern Kazakhstan. J. Geophys. Res. 107 (B7), 2139. http://dx.doi.org/10.1029/2001JB000521.

McCuaig, T.C., Kerrich, R., 1998. P-T-t-deformation-fluid characteristics of lode gold deposits: evidence from alteration systematics. Ore Geol. Rev. 12, 381–453.

Müller, W., Shelley, M., Miller, P., Broude, S., 2009. Initial performance metrics of a new custom-designed ArF excimer LA-ICPMS system coupled to a two-volume laser-ablation cell. J. Anal. At. Spectrom. 24, 209–214.

Naumov, E., Borisenko, A., Kovalev, K., Kalinin, Y., Seltmann, R., 2012. Gold Deposits of Ob-Zaisan Fold Zone (Western Siberia and Eastern Kazakhstan): Types and Ages of Mineralization Correlation with Magmatic Complexes [abs.], 34th International Geological Congress, Brisbane, Australia Abstract.

Nordgold, 2015. Ore Reserves and Mineral Resources Summary. Retrived from http://www.nordgold.com/operations/production/suzdal/.

Pitcairn, I.K., Teagle, D.A.H., Craw, D., Olivo, G.R., Kerrich, R., Brewer, T.S., 2006. Sources of metals and fluids in orogenic gold deposits: insights from the Otago and Alpine Schists, New Zealand. Econ. Geol. 101, 1525–1546.

Pitcairn, I.K., Craw, D., Teagle, D.A.H., 2015. Metabasalts as sources of metals in orogenic gold deposits. Mineral. Deposita 50, 373–390.

Pourcelot, L., Vintró, L.L., Mitchell, P.I., Burkitbayev, M., Uralbekov, B., Bolatov, A., Strilchuk, Y., Métivier, J.M., Priest, N.D., 2014. Hydrological behaviour of tritium on the former Semipalatinsk nuclear test site (Kazakhstan) determined using stable isotope measurements. Eurasian Chem. Technol. J. 15, 293–299.

Ridley, J.R., Diamond, L.W., 2000. Fluid chemistry of orogenic lode gold deposits and implications for genetic models. Rev. Econ. Geol. 13, 141–162.

Safonova, I.Y., Simonov, V.A., Kurganskaya, E.V., Obut, O.T., Romer, R.L., Seltmann, R., 2012. Late Paleozoic oceanic basalts hosted by the char suture shear zone, East Kazakhstan: geological position, geochemistry, petrogenesis and tectonic setting. J. Asian Earth Sci. 49, 20–39.

Seal II, R.R., 2006. Sulfur isotope geochemistry of sulfide minerals. Rev. Mineral. Geochem. 61, 633–677.

Sengör, A.M.C., Natal'in, B.A., Burtman, V.S., 1993. Evolution of the altaid tectonic collage and Paleozoic crustal growth in Eurasia. Nature 364, 299–307.

Shen, P., Pan, H., Seitmuratova, E., Jakupova, S., 2016. U–Pb zircon, geochemical and Sr–Nd–Hf–O isotopic constraints on age and origin of the ore-bearing intrusions from the Nurkazgan porphyry Cu–Au deposit in Kazakhstan. J. Asian Earth Sci. 116, 232–248.

Sheppard, S., 1986. Characterization and isotopic variations in natural waters. Rev. Mineral. Geochem. 16, 165–183.

Thomas, H.V., Large, R.R., Bull, W.W., Maslennikov, V., Berry, R.F., Fraser, R., Froud, S., Moye, R., 2011. Pyrite and pyrrhotite textures and composition in sediments, laminated quartz veins, and reefs at Bendigo gold mine, Australia: insights for ore genesis. Bull. Soc. Econ. Geol. 106, 1–31.

Thompson, J.F.H., Sillitoe, R.H., Baker, T., Lang, J.R., Mortensen, J.K., 1999. Intrusion-related gold deposits associated tungsten-tin provinces. Mineral. Deposita 34, 323–334.

Tomkins, A.G., 2010. Windows of metamorphic sulfur liberation in the crust: implications for gold deposit genesis. Geochim. Cosmochim. Acta 74, 3246–3259.

Travin, A.V., Boven, A., Plotnikov, A.V., Vladimirov, V.G., Theunissen, K., Vladimirov, A.G., Melnikov, A.I., Titov, A.V., 2001. Ar-40/Ar-39 dating of ductile deformations in the Irtysh shear zone, eastern Kazakhstan. Geochem. Int. 39, 333–346.

Vladimirov, A.G., Kruk, N.N., Khromykh, S.V., Polyansky, O.P., Chervov, V.V., Vladimirov, V.G., Travin, A.V., Babin, G.A., Kuibida, M.L., Khomyakov, V.D., 2008. Permian magmatism and lithospheric deformation in the Altai caused by crustal and mantle thermal processes. Russ. Geol. Geophys. 49, 468–479.

Volkova, N.I., Tarasova, E.N., Polyanskii, N.V., Khomyakov, V.D., 2008. High pressure rocks in the serpentinized mélange of the chara zone, East Kazakhstan: geochemistry, petrology and age. Geochem. Int. 46, 386–401.

Wang, Y.H., Xue, C.J., Zhang, F.F., Liu, J.J., Gao, J.B., Qi, T.J., 2015. SHRIMP zircon U–Pb geochronology, geochemistry and H–O–Si–S–Pb isotope systematics of the Kanggur gold deposit in Eastern Tianshan, NW China: implication for ore genesis. Ore Geol. Rev. 68, 1–13.

Wilde, A.R., Layer, P., Mernagh, T., Foster, J., 2001. The giant Muruntau gold deposit geologic, geochronologic, and fluid inclusion constraints on ore genesis. Econ. Geol. 96, 633–644.

Windley, B.F., Alexeiev, D., Xiao, W., Kroner, A., Badarch, G., 2007. Tectonic models for accretion of the Central Asian orogenic belt. J. Geol. Soc. Lond. 164, 31–47.

Yuan, W., Carter, A., Dong, J., Bao, Z., An, Y., Guo, Z., 2006. Mesozoic–tertiary exhumation history of the Altai Mountains, northern Xinjiang, China: new constraints from apatite fission track data. Tectonophysics 412, 183–193.

Yuan, H.L., Chen, K.Y., Bao, Z.A., Zong, C., Dai, M., Fan, C., Yin, C., 2013. Determination of lead isotope compositions of geological samples using femtosecond laser ablation MC-ICP-MS. Chin. Sci. Bull. 58 (32), 3914–3921.

Yuan, H.L., Yin, C., Liu, X., Chen, K.Y., Bao, Z.A., Zong, C.L., Dai, M.N., Lai, S.C., Wang, R., Jiang, S.Y., 2015. High precision in-situ Pb isotopic analysis of sulfide minerals by femtosecond laser ablation multi-collector inductively coupled plasma mass spectrometry. Sci. China Earth Sci. 58, 1713–1721.

Zartman, R.E., Haines, S.M., 1988. The plumbotectonic model for Pb isotopic systematics among major terrestrial reservoirs — a case study for bi-directional transport. Geochim. Cosmochim. Acta 52, 1327–1339.

Zhong, R., Brugger, J., Tomkins, A.G., Chen, Y., Li, W., 2015. Fate of gold and base metals during metamorphic devolatilization of a pelite. Geochim. Cosmochim. Acta 171, 338–352.